Asia-Pacific Journal of Science and Technology: Volume: 29. Issue: 04. Article ID.: APST-29-04-11. Research Article

APST

Asia-Pacific Journal of Science and Technology

https://www.tci-thaijo.org/index.php/APST/index

Published by the Research and Graduate Studies,
Khon Kaen University, Thailand

Green synthesis of NiO nanoparticles from maize waste for cationic dye degradation

Jagadeeswari Rangaraman[1,*], Rathika Govindasamy[2], Selvakumar Ponnusamy[3] and Saranya Jagadeesan[3]

[1]Department of Chemistry, KPR Institute of Engineering and Technology, Tamil Nadu India
[2]Department of Chemistry, PSG College of Arts & Science, Tamil Nadu, India
[3]Department of Humanities and Sciences, Gokaraju Rangaraju Institute of Engineering and Technology, Telangana, India
[*]Corresponding author: r.jagadeeswari@kpriet.ac.in

Received 7 June 2023
Revised 4 July 2023
Accepted 10 August 2023

Abstract

The current work investigates the green synthesis of nickel oxide nanoparticles (GNiO NPs) derived from its nickel salt using maize waste as a reducing agent. The formation of GNiO NPs was confirmed by techniques such as Fourier transform infrared (FTIR) spectroscopy, x-ray diffraction (XRD) and ultraviolet-visible diffuse reflectance spectroscopy (UV-DRS). The analysis of UV-DRS spectra indicates an optical band gap of 3.15 eV for the newly formed GNiO NPs. Meanwhile, Rietveld refinements performed using the GSAS package confirm the formation of the face-centered cubic structures with a lattice parameter of 4.173 Å. The scanning electron microscopy (SEM) examination reveals that the as-prepared GNiO NPs have an average size of 41 nm. In addition, energy-dispersive x-ray (EDX) spectroscopy analysis indicates that the GNiO NPs are highly pure and do not contain any impurities. Subsequently, the as-synthesized GNiO NPs are employed as the photocatalyst for the degradation of cationic dyes under UV radiation. The photocatalytic degradation efficiency of GNiO NPs towards MB is found to be 85.27%, whereas for RhB it is slightly lower at 74.81%. The photodegradation rate for both dyes follows a pseudo-first-order kinetics with rate constants of 0.0258 min^{-1} and 0.0213 min^{-1}, respectively.

Keywords: Green synthesis, Maize waste, Methylene blue, NiO nanoparticles, Photodegradation, Rhodamine-B

1. Introduction

Nanosized nickel oxide (NiO) has garnered significant attention as a promising transition metal oxide with diverse applications electrochemical supercapacitors, superparamagnetic devices, photocatalysis and magnetic devices [1]. Characterized by a broad bandgap (3.6-4.0 eV) and a high exciton binding energy, these nanoparticles (NPs) are identified as p-type semiconductors. Bulk NiO lacks magnetism and its Neel temperature is just 523K [2]. However, owing to their quantum size and surface effects, nanosized NiO particles exhibit a wide variety of characteristics including optical, electrical, chemical, and magnetic properties that distinguish them from bulk counterparts [3].

Dyes have been used in the production of various substances for decades. These are not only essential to the textile sector but also by several other sectors which include pulp, food, paper, leather, cosmetics, and more. These sectors are the most consistent water consumers, and as a result, they are responsible for a disproportionately large amount of water contamination that goes untreated. Discharging untreated dye into water reservoirs poses a threat to aquatic species, human health and the environment [4]. In recent years, researchers around the world have placed a high priority on dye removal before releasing industrial dyes-based wastewater [5], employing methods such as adsorption, biological discolouration, AOP (Advanced Oxidation Processes) like the Photo-Fenton reaction and photocatalytic degradation [6]. Nevertheless, the catalytic reactions of NiO NPs differ due to differences in their ability to generate reactive oxygen species (ROS) and the specific types of ROS they generate. This highlights that the preparation of these NPs is equally crucial as their physico-chemical features (size, shape, and surface area) in determining catalytic outcomes [7].

Furthermore, several techniques were employed to prepare NiO nanoparticles, encompassing thermal decomposition, sol-gel procedure, green approaches, and polymer-matrix aided synthesis [8]. The green method specifically involves the use of plant parts and their wastes for preparation of nanoparticles, incorporating chemical constituents such as flavonoids, phenols, proteins, steroids, carbohydrates, glycosides, terpenoids, tannins, alkaloids, vitamins, mineral elements, and a myriad of other chemical compounds [9]. In addition, NiO prepared via the green approach has also been reported in a few publications for applications in photocatalysis [10]. The grass family (Poaceae) includes maize, or *Zea mays* and because of its high nutritional content and practicality as a source of energy, maize (*Zea mays* L.), is one of the most popular and extensively eaten staple nutrients all over the world [11]. While there are quite a few papers on the preparation of metal oxide nanoparticles such ZnO, PbS, TiO_2, CuO, Ag, etc. from corn cob waste [12]. Herein, we present a straightforward green method for synthesizing nanocrystalline NiO from its nickel salt using maize waste. Structural and morphological characterization were conducted using Fourier transform infrared (FTIR), scanning electron microscopy-energy-dispersive x-ray (SEM-EDX), ultraviolet-visible diffuse reflectance spectroscopy (UV-DRS) and x-ray diffraction (XRD) analyses. Subsequently, the resulting green synthesis of nickel oxide nanoparticles (GNiO NPs) were employed as a photocatalyst for the degradation of cationic dyes (methylene blue (MB) and rhodamine B (RhB)) under UV radiation and their efficiency was examined.

2. Materials and methods

2.1 Materials

Analytical reagent (AR) grade nickel nitrate, rhodamine b, and methylene blue were acquired from Merck Specialties Private Limited, Mumbai and used without further purification. The water employed for preparing all solutions in the experiments underwent double distillation.

2.2 Preparation of maize waste extract

Corn on the cob, with the kernels and husk still attached, was purchased from a local vendor in Coimbatore, Tamil Nadu, India. Approximately, 50 g of raw broken husk was carefully removed from the cob, rinsed in deionized water and subsequently placed in 180 mL of sterile water. The mixture was then heated to 60°C for 3 h, yielding a mild yellow colored extract. The collected extract had a pH of 4. In another method, the corn husk was dried at 40°C and crushed it to powder. An extract was made by boiling 20 g of powdered dry maize husk in distilled water (200 mL) for 2 h at 60°C. Lastly, another extract was obtained by boiling 10 g of fresh maize silk in 200 mL deionized water at 60°C for 3 h. All the extracts were mixed, allowed to cool to laboratory temperature, and then filtered using Whatman filter paper. The filtered extract is stored in the refrigerator at 4°C for further studies.

2.3 Synthesize of green NiO NPs

In order to prepare the NiO NPs, 25 mL of the prepared maize extract was gradually heated using a stirrer-heater, following the methodology outlined in earlier published research [12]. At 60°C, a 0.1M aqueous solution of $Ni(NO_3)_2.6H_2O$ was added drop by drop to the mixture. The mixture was stirred for 6 h at 80°C resulting in the formation of a green-coloured precipitate. To eliminate impurities, the precipitate underwent multiple washing with distilled water and ethanol. Thereafter, the precipitate was dried at 120°C before being annealed at 600°C for 5 h with a temperature raise of 10°C/min.

2.4 Characterization and measurements

The crystal structure of GNiO NPs was determined through x-ray diffraction (XRD) analysis utilizing an x-ray diffractometer (Rigaku D max-C) with CuKα radiation (1.5406 Å). Structural and chemical compositions analyses were carried out using a scanning electron microscope (SEM with EDX, Sirion). Gwyddion, a freely available software, was used for surface roughness analysis. Additionally, the SEM images of GNiO NPs were converted to 3D with the help of Gwyddion 2.58. Mean roughness (Ra), mean square roughness (Rq), surface skewness (Rsk), and kurtosis coefficient (Rku) were then calculated to characterize the surface's roughness [13]. The optical absorption spectra of NPs were recorded using a UV-DRS spectrophotometer (JASCO V-750).

2.5 Photocatalytic studies

A photocatalytic reactor system featuring a wooden chamber was employed for the photodegradation testing. The wooden box housed a 15 W UV lamp (Philips TUV-08) with an emitting wavelength at 365 nm. In a 30 mL

aqueous solution of dye (RhB/MB) with a concentration of 1×10^{-5} M, 0.03 g of GNiO NP catalyst was dissolved. To achieve adsorption equilibrium, the solution was stirred for 10 min and then left undisturbed for 1 h in dark. Afterward, 5 mL of the sample solution was introduced to a photoreactor and exposed to UV light for photodegradation. Dye concentrations in the solutions were calculated at room temperature using a standard curve based on the optical absorption, measured via a UV-Vis spectrophotometer. The maximum peak intensity is measured at λ_{max} = 663 nm (MB) and λ_{max}=554 nm (RhB), and it gradually decreases between 0 and 60 min of exposure to UV light. The degradation effectiveness was determined using the formula [10].

$$\% \text{ Degradation } (\eta) = [1 - C_t/C_0] \times 100 \quad (1)$$

where C_0 is the initial concentration of the dye and Ct is the concentration of dye solution at different time interval.

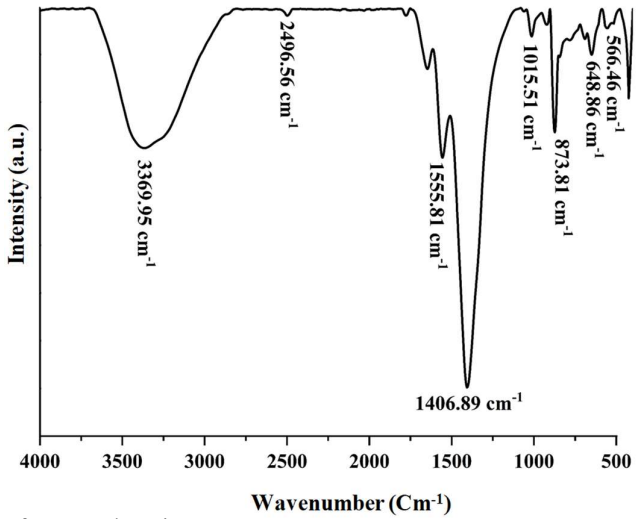

Figure 1 FTIR spectra of prepared GNiO NPs.

3. Results and discussion

Maize waste has been shown to contain significant levels of phenolic and flavonoid compounds, demonstrating their utility in the bio-reduction and ecofriendly production of metal oxide NPs through bio-reduction processes [14]. The positively charged Ni^{2+} complex ions are stabilized by the donation of electrons from negatively charged phenolic and flavonoid groups present in maize waste. In this process, Ni^{2+} ions undergo reduction to Ni^0 and upon calcination at 500°C, they are further converted into NiO NPs. The possible chemical reaction is as described below.

$$\text{Maize waste extract} + Ni^{2+} \longrightarrow [\text{Maize waste extract}/Ni^{2+}]$$

$$[\text{Maize waste extract}/Ni^{2+}] + O_{2(g)} \longrightarrow \text{NiO NPs} + CO_{2(g)}$$

3.1 FTIR

To discern the most prominent chemical bonding in GNiO NPs, FTIR measurements were conducted under laboratory conditions, and the resulting spectra are presented in Figure 1. The spectrum showed two peaks at 566.46 cm^{-1} and 642.68 cm^{-1}, likely originating from the stretching vibrations of Ni-O bond. The crystalline structure of the GNiO NPs was evident from the broadness of the peaks, with sharp peaks clearly indicating their crystalline nature. The absorption at 2496.56 cm^{-1} was attribute to CO_2 molecules resonating in their symmetric and asymmetric stretching modes after being absorbed by GNiO NPs from the surrounding air [15]. During FTIR analysis, stretching and bending vibrations of the -OH group, which may account for the broad peak at 3369.95 cm^{-1}, 1406.89cm^{-1}, and 1555.81 cm^{-1}, this may be due to the catalyst's surface absorbs environmental water [16].

3.2 UV-DRS

Figure 2 (A) depicts the results of UV-DRS measurements conducted on GNiO NPs within the wavelengths range of 200 to 800 nm. The absorption spectra obtained through UV-DRS revealed a broad peak spanning from 200 to 400nm, and the optical band gap of the resulting materials was calculated using Tauc's Equation [17].

$$[F(R)h\upsilon/t]^{1/n} = A\,(h\upsilon - E_g) \quad (2)$$

Material thickness (t), spectral reflectance (R), band gap transition (n), a proportionality constant (A), and photon energy (h) represents the Kubelka-Munk function ($F(R) = (1\,R)^2/2R$). Tauc plotted the connection between $h\upsilon$ and $[F\,(R)h]^2$, the tangent line drawn to meet the x-axis (Figure 2B). The energy band gap (E_g) for GNiO NPs was determined to be 3.15 eV based on the data shown in the image. The zero-charge valence band (VB) edge potential of a semiconductor may be calculated using the following Equation.

$$E_{VB} = X - E^C + 0.5\,E_g \quad (3)$$

where E_g- semiconductor band gap energy, X- materials electronegativity, E^c-energy of hydrogen scale free electrons (4.5 eV), and E_{VB} is the VB edge potential. The edge potential of the conduction band (E_{CB}) is found by solving for $E_{CB} = E_{VB} - E_g$. GNiO NPs has an E_{VB} of 3.66 eV and an E_{CB} of 0.51 eV; its X value is around 6.585. Band gap and blue shifts observed in the UV-vis spectrum are significant indicators that the GNiO NPs particle size has decreased.

3.3 Powder x-ray diffraction (PXRD)

PXRD is a vital technique for identifying the composition, structure, elemental phase, and type of elements within a sample, especially nanopowders. Furthermore, PXRD information allows for the calculation of crystallite size in the sample. Figure 3 shows the PXRD pattern of the as-prepared GNiO NPs, which was recorded with 2θ values between 20° to 80°. The observed PXRD pattern was in a good agreement with JCPDS card no.00-004-0835 [18], since its peaks appear at 2θ values of 37.26^0, 43.31^0, 62.9^0, 75.42^0, and 79.38^0, corresponding to the planes (111), (200), (220), (311), and (222). Based on these results, it was inferred that the NiO was present in the nanophase and exhibited a cubic crystal structure.

The prepared GNiO NPs are crystalline, as shown by the strength and sharpness of the peaks. Further, the nonappearance of other peaks proposes that the as-prepared GNiO NPs are very pure. As-prepared GNiO NPs has an average crystallite size of 41 nm, as calculated using Scherrer formula [19]:

$$D = \frac{K\lambda}{\beta\cos\theta} \quad (4)$$

'D' mean crystallite size, 'λ' incident wavelength (1.540 Å, Cu Kα), K-shape factor (0.89), 'β'-full width at half maximum, and 'θ'-diffraction angle. Applying the formula presented below [20]

$$\delta = \frac{1}{D^2} \quad (5)$$

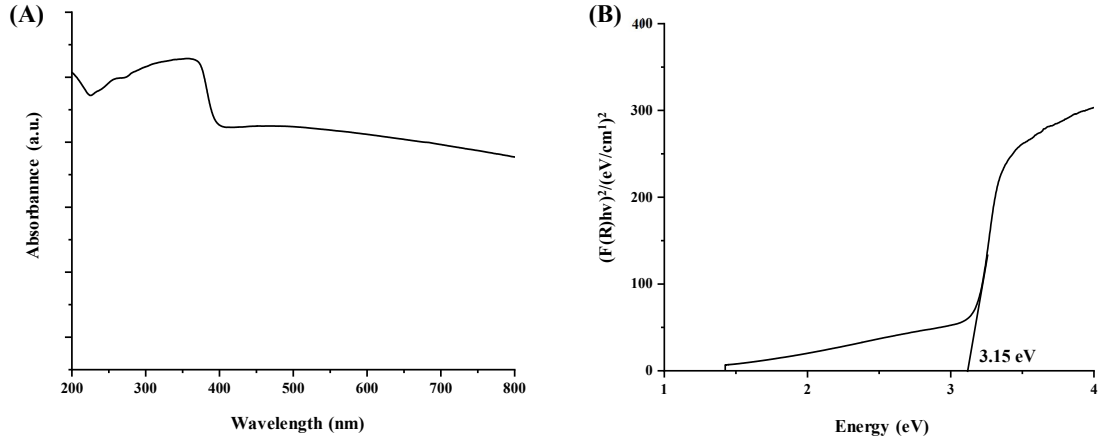

Figure 2 (A) UV-DRS and (B) bandgap spectra of prepared GNiO NPs

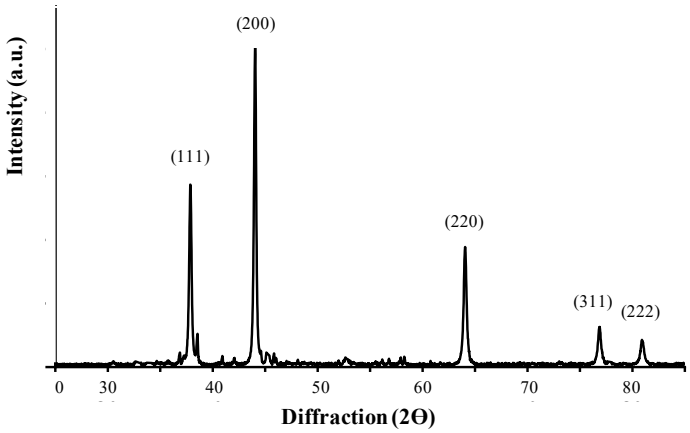

Figure 3 XRD spectra of prepared GNiO NPs.

The density of dislocations (δ) was calculated to be 3.7×10^{15}. From the PXRD analysis, strain may also be determined using the Williamson-Hall (W-H) formula ($\varepsilon = \beta\cos(\theta)/4$). Hooke's law ($\sigma = C\varepsilon$) allows us to get stress values from strain. Where 'C' stands for the bulk Young's modulus (1.46 ± 10^{10} N/m^2). Micro-strain and micro-stress values for the produced GNiO NPs are determined to be 0.0035 and 46.8 MPa, respectively. The higher strain value contributed to an increase in the lattice constant values, a decrease in particle size, and minor shifts in XRD peaks. Consequently, the structural defects emerged due to disorder which included broken bonds thereby improving the catalytic abilities of GNiO NPs. Above results correlates well with the previous published result [21].

The Rietveld refinement method [22] may be used in conjunction with features of the XRD pattern, such as peak shift, peak broadening, peak asymmetry, etc., to assess the crystal structure of the material under study. In this study, GSAS-II programme was used to conduct Rietveld refinement on experimentally acquired XRD data in order to assess the influence of the synthesis process on structural parameters (Figure 4). The data was refined using the Marquardt least squares method, which helps bring the discrepancy between the estimated and experimental pattern down to a manageable level. The method relies on the integrated diffraction peaks as a function of structural features.

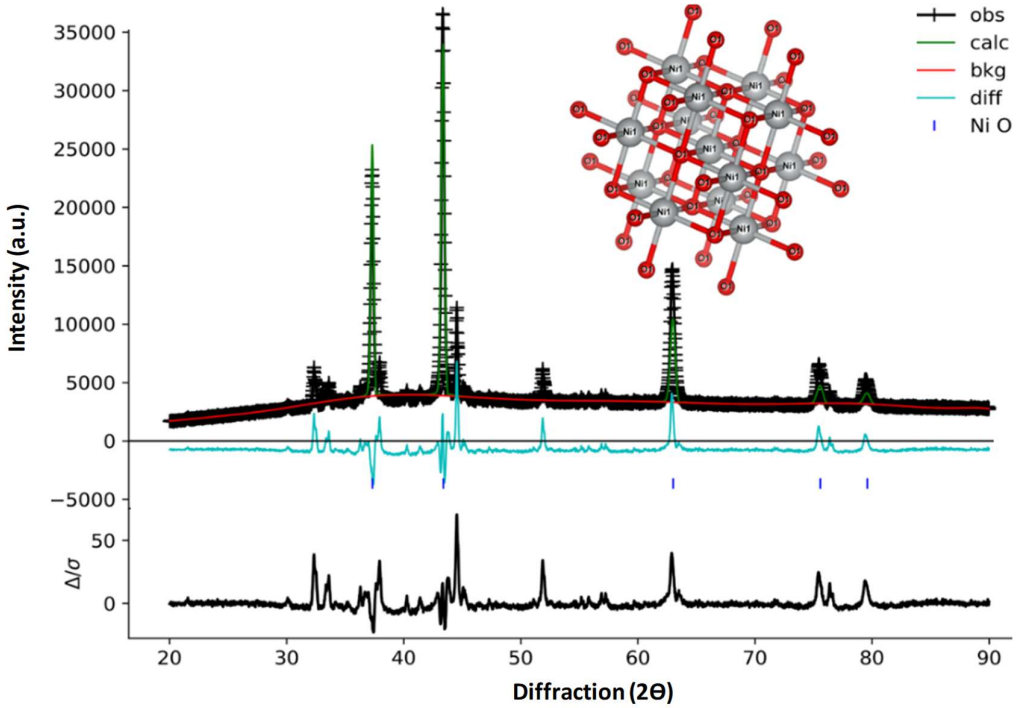

Figure 4 Rietveld refinement of prepared GNiO NPs.

All the measured peaks aligned extremely well with the acceptable Bragg 2θ positions for the Fm-3m space group, demonstrating unequivocal evidence that the synthesized sample was pure NiO NPs and existed in a single phase [24]. Figure 4 depicts the Rietveld refined data for an XRD pattern using GSAS, where the black line represents the experimental data, the solid green line corresponds to the calculated intensities, and the line at the bottom indicates the difference between measured and calculated intensities. The vertical lines signify the allowed Bragg's positions for the Fm-3m space group. The goodness-of-fit, R-factor, and weighted-profile R-factor values were small ($\chi^2 = 4.1$), (Rp = 11.41) and (Rwp = 15.54) respectively, representing that all synthesized GNiO NPs were face-centered cubic crystals of the same phase with lattice parameters of a = b = c = 4.173 Å. A χ^2 value of 1 indicates a perfect model with accurate standard uncertainty (s.u) values. are accurate. The parameters with the minimum values best fit the experimental diffraction data [25].

3.4 The scanning electron microscopy energy dispersive x-ray (SEM-EDS)

The GNiO NP SEM images are presented in Figure 5 (A). Particle agglomeration resulted in irregularly shaped spheres with variations in size, as apparent in the SEM images. The effectiveness of GNiO NPs as a photocatalyst was attributed to their larger surface area [23]. Figure 5 (B) shows a three-dimensional rendition of a scanning electron micrograph of GNiO NP, a nanoparticle catalyst having growth sites on its surface. In addition, pointed cone-shaped crystallites were observed. Furthermore, Figure 6 depicts the EDX of GNiO NPs where the synthesized NPs can be easily identified as composed Ni and O. Since no other contaminants were found in the sample spectrum, this confirms the purity of the GNiO NPs. The exact atomic ratios of Ni to O are 67.3% (Ni) to 32.6% (O).

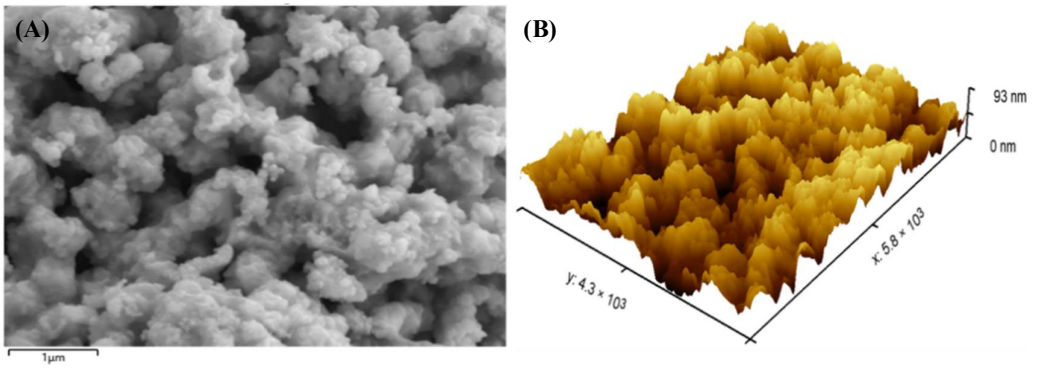

Figure 5 (A) SEM images and (B) surface view of prepared GNiO NPs.

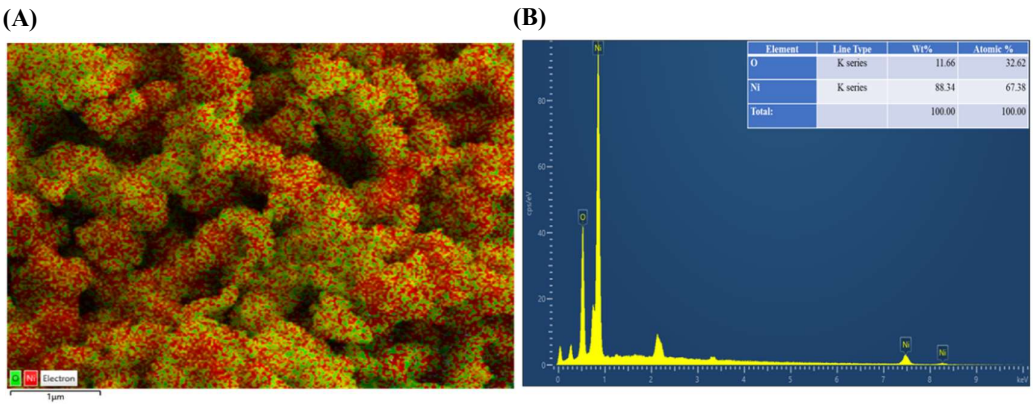

Figure 6 (A) EDX spectra and (B) elemental mapping of prepared GNiO NPs.

3.5 Surface roughness

The specific surface area of a substance plays a pivotal role in determining its usefulness. The Brunauer-Emmett-Teller (BET) isotherm model is used to estimate this parameter by analyzing the adsorption of a probing gas sorbate. Here, 'BET surface area' refers to the product of the adsorbate's molecular cross-sectional area and the BET monolayer capacity. The utilization of BET surface area is frequent, yet its validity and accuracy subject to question [24], primarily due to the discrepancy in surface areas obtained when probing with sorbates like nitrogen and water. On the other hand, SEM was used to analyze number-weighted size distributions of

nanoparticles by individually identifying them and observing their shapes. It is noteworthy that the shape of NPs determined the threshold of the volume-specific surface area acquired for the BET surface area via gas adsorption. The problem can be mitigated by employing image characterization through Gwyddion and considering SEM data. This approach allows for the establishment of statistical characteristics related to surface porosity and surface roughness, along with the generation of 3-d reconstructions.

Table 1 Surface roughness parameters of GNiO NPs.

Parameters	NiO (nanometers)
Average roughness (Ra)	40.7
Root mean square roughnessv (Rq)	51.4
Roughness maximum (Rt)	367.6
Valley depth of roughness maximum (Rv)	140.8
Height of roughness maximum (Rp)	156.5
Roughness maximum height (average) (Rtm)	276.8

Both surface area and structure influence of GNiO NPs enhances photocatalytic activity (Table 1). When UV-DRS readings are included in, the bandgap energy barely varies by a little amount (3.15 eV) from the bulk. Therefore, shape is crucial since it increases surface area. The SEM findings on surface roughness also provide advantages to GNiO NPs superior activity. Adsorption is the first step in the photocatalytic process, and it is facilitated by the roughness of the catalyst's surface, which is high because low crystallinity results in less atomic arbitrary, leading to Ra around 40.7 nm and Rp around 156.5 nm. Therefore, the results of this investigation demonstrate unequivocally the significance of particle size, surface area, and shape to the photocatalytic activity of the produced catalyst.

3.6 Photocatalytic degradation of MB and RhB

The photocatalytic performance of GNiO NPs under UV light was studied by exposing it to RhB and MB dyes. Figure 7 shows the gradual breakdown of cationic dyes by GNiO NPs over time. Absorption spectra typically show a steady weakening of the MB absorption peak around 663 nm and for RhB absorption peak around 554 nm. After 60 min of exposure to UV radiation, almost all the MB dye was destroyed in the presence of GNiO NPs. As illustrated in Figure 7 GNiO NPs demonstrate a maximum degradation rate of 85.27% for MB after 60min, while the rate for RhB dye was slightly lower at 74.81% after 60 min. The increased photocatalytic activity of GNiO NPs could be plausibly explained by their larger total surface area [25].

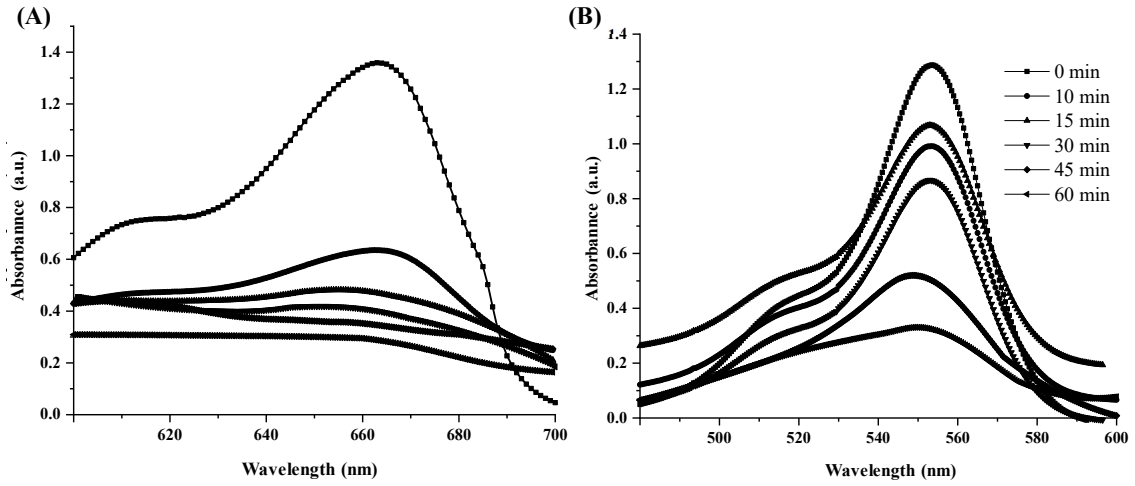

Figure 7 Degradation of (A) MB dye and (B) RhB dye under UV light by GNiO NPs.

This measures the surface area of the photocatalyst that is capable of generating free radicals [26]. The semiconductor's reduced band gap enables it to capture more photons, which excites electrons from the VB (valence band)-CB (conduction band), contributing to the enhancement of photocatalytic activity [3]. The photocatalytic activity is also affected by the transition metal and semiconductor material's electronic band structure arrangement. These results suggest that the surface roughness of the GNiO NP material is critical to the degradation of dyes. Further, the high selectivity of photodegradation is largely influenced by photosensitization of dyes. Notably, RhB and MB exhibited different highest occupied molecular orbital (HOMO) energy gaps with

-10.494 eV for MB and -10.128 eV for RhB [27]. The increased degradation rate of MB compared to RhB may be explained by the fact that the electrons were more easily transported to the photocatalyst.

3.7 Degradation mechanism and kinetic study

When UV light transmitted on a GNiO surface, electrons in the valence band (the lowest energy level) gather enough kinetic energy to jump to the conduction band. The amount of energy required is equal to the bandgap energy of the nanomaterial. According to the UV-DRS analysis, GNiO has an E_{bg} of 3.15 eV. So, when excited, valence band holes may freely react with water molecules to produce OH free radicals, which can then repeatedly attack the target chemical moiety (RhB & MB), eventually destroying it. The correlation between concentration shifts and response time (in minutes) for cationic dyes are shown in Figure 8.

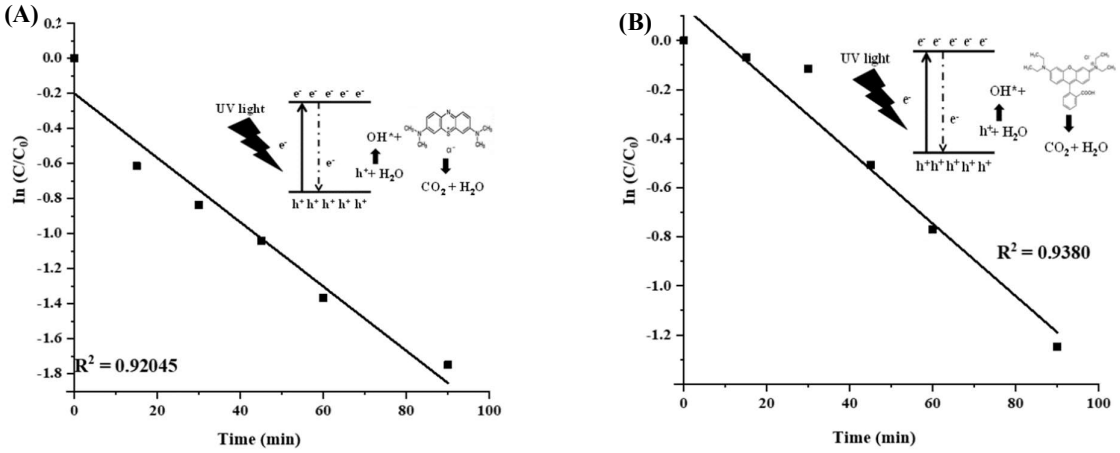

Figure 8 Pseudo first order kinetics for the photocatalytic degradation of (A) MB and (B) RhB under UV light by GNiO NPs.

The rate constant for this degradation process is calculated using the following formula [2], and the kinetics are of pseudo-first order.

$$\ln\left[\frac{C}{C_0}\right] = kt \tag{6}$$

Figure 8 shows a graph of In(C/Co) vs reaction time from which the R^2 value and the rate constant (k) are computed to be 0.9204; 0.9380 and 0.0258 min^{-1}; 0.0213 min^{-1} for MB and RhB, respectively.

Table 2 Comparison of GNiO NP's photocatalytic activity with reported literature.

Material	Reductant/ Dopant	Dye	Light source	Time (min)	% Removal	Rate constant	References
CuO	Maize cob	MB	UV	150	91.00	0.02582	[28]
SnO_2	Corncob activated carbon	MB	Sunlight	120	90.86	0.02000	[29]
ZnO	Maize biochar	Saf-O MC	Sunlight	60 50	87.00 57.00	0.8820 0.9200	[30]
NiO	Sutherlendia frutescene	MB MG	UV	270 210	86.00 98.00	- -	[3]
NiO	NH_3	MB	Sunlight	120	80.00	-	[21]
NiO	Tragacanth	MB	UV	300	60.00	0.0280	[10]
NiO	Maize waste	MB RhB	UV	60	85.27 74.81	0.0258 0.0213	This work

Table 2 presents a comparative analysis showcasing GNiO NPs in relation to earlier published reports concerning the preparation process, the utilized light source, the degradation, and kinetics associated with dye degradation. The majority of these particles were produced using an environmentally friendly process and demonstrated a particle size of 50 nm or less. Optimal conditions for their degradation capacity involved UV light

as the preferred light source, with a typical exposure time ranging between 120 and 150 min. This suggested that phytochemicals produced by the plant may exert a bigger effect on the structural parameters and degradation ability of GNiO NPs proved to be highly effective photocatalyst, as evidenced by complete degradation within 60 min, possibly ascribed to the increased surface area of the nanosized particles.

4. Conclusion

Finally, the structure and morphology of GNiO NPs were investigated using a physicochemical approach (PXRD, UV-DRS, SEM, EDX, and FTIR measurements). The findings demonstrated successful synthesis of GNiO NPs utilizing waste maize extract as a natural reducing agent. SEM analysis corroborated the average particle size range of 41nm as identified by PXRD studies. EDX analysis confirmed the presence of Ni and O, indicating the synthesis of pure GNiO NPs with a Ni/O ratio of approximately 1:1. Moreover, the calculated optical band gap of 3.15 eV was consistent with the formation of GNiO particles at nanoscale. Rietveld refinement revealed the cubic crystal structure with the point group Fm-3m. Further investigation into the particle size and narrow band gap of GNiO NPs was conducted through SEM imaging using Gwyddion, providing surface characteristics with Ra (40.7 nm) and Rq (51.4 nm). The as-prepared GNiO NPs were shown to be efficient in precipitating RhB (74.81%) and MB (85.27 %) dyes from aqueous solutions. It was further observed that MB dye demonstrated superior degradation through photocatalysis compared to RhB, giving it an edge over RhB.

5. References

[1] Berhe MG, Gebreslassie YT. Biomedical applications of biosynthesized nickel oxide nanoparticles. Int J Nanomedicine. 2023;18:4229-4251.

[2] Meer H, Gomonay O, Wittmann A, Kläui M. Antiferromagnetic insulatronics: spintronics in insulating 3d metal oxides with antiferromagnetic coupling. Appl Phys Lett. 2023;122(8):080502.

[3] Motene K, Glory MLM, Ngoepe NM, Mathipa MM, Mbita HNC. Photocatalytic degradation of dyes and removal of bacteria using biosynthesised flowerlike NiO nanoparticles. Int J Environ Anal Chem. 2023; 103:1107-1122.

[4] Ahmed J, Thakur A, Goyal A. Industrial wastewater and its toxic effects. In: Shah MP, editor. Biological treatment of industrial wastewater. 1st ed. London: The Royal Society of Chemistry; 2021. p.1-14.

[5] Durodola SS, Akeremale OK, Ore OT, Bayode AA, Badamasi H, Olusola JA. A review on nanomaterial as photocatalysts for degradation of organic pollutants. J Fluoresc. 2023:1-14.

[6] Haleem A, Shafiq A, Chen SQ, Nazar M. A comprehensive review on adsorption, photocatalytic and chemical degradation of dyes and nitro-compounds over different kinds of porous and composite materials. Molecules. 2023;28:1081.

[7] El-Kady MM, Ansari I, Arora C, Rai N, Soni S, Verma DK, et al. Nanomaterials: a comprehensive review of applications, toxicity, impact, and fate to environment. J Mol Liq. 2022:121046.

[8] Zegebreal LT, Tegegne NA, Hone FG. Recent progress in hybrid conducting polymers and metal oxide nanocomposite for room-temperature gas sensor applications: a review. Sens Actuators Phys. 2023;359:114472.

[9] Bachheti RK, Bachheti A, editors. Secondary metabolites from medicinal plants: nanoparticles synthesis and their applications. 1st ed. CRC Press; 2023.

[10] Sabouri Z, Akbari A, Hosseini HA, Khatami M, Darroudi M. Tragacanth-mediate synthesis of NiO nanosheets for cytotoxicity and photocatalytic degradation of organic dyes. Bioprocess Biosyst Eng. 2020; 43:1209-1218.

[11] Hussain S, Ijaz M, Hussain M, Ul-Allah S, Abbas T, Nawaz A, et al. Advanced production technologies of maize. In: Hasanuzzaman M, editor. Agronomic crops. 1st ed. Singapore, Springer; 2019.p.237-260.

[12] Adebisi JA, Agunsoye JO, Bello SA, Haris M, Ramakokovhu MM, Daramola MO, et al. Green production of silica nanoparticles from maize stalk. Part Sci Technol. 2020;38:667-675.

[13] Trovato V, Mezzi A, Brucale M, Abdeh H, Drommi D, Rosace G, et al. Sol-Gel Assisted immobilization of alizarin red s on polyester fabrics for developing stimuli-responsive wearable sensors. Polymers. 2022; 14:2788.

[14] Ebrahimian J, Mohsennia M, Khayatkashani M. Catalytic and photocatalytic activity of *Urtica dioica*-mediated Ud-ZnO nanoparticles. Opt Mater. 2021;120:111404.

[15] Al-Ghamdi SA, Alkathiri TA, Alfarraj AE, Alatawi OM, Alkathiri AS, Panneerselvam C, et al. Green synthesis and characterization of zinc oxide nanoparticles using Camellia sinensis tea leaf extract and their antioxidant, anti-bactericidal and anticancer efficacy. Res Chem Intermed. 2022;48:4769-4783.

[16] Saka A, Tesfaye JL, Gudata L, Shanmugam R, Dwarampudi LP, Nagaprasad N, et al. Synthesis, characterization, and antibacterial activity of ZnO nanoparticles from fresh leaf extracts of Apocynaceae, *Carissa spinarum* L. (Hagamsa). J Nanomater. 2022;2022:1-6.

[17] Ghiyasi Y, Salahi E, Esfahani H. Synergy effect of *Urtica dioica* and ZnO NPs on microstructure, antibacterial activity and cytotoxicity of electrospun PCL scaffold for wound dressing application. Mater Today Commun. 2021;26:102163.
[18] Abioye AM, Abdulkadir LN, Ani FN. Effect of calcination conditions on the supercapacitive performance of activated carbon/nickel oxide nanocomposite electrodes prepared by electroless nickel plating. J Electron Mater. 2019;48:3721-3735.
[19] Abioye AM, Noorden ZA, Ani FN. Synthesis and characterizations of electroless oil palm shell based-activated carbon/nickel oxide nanocomposite electrodes for supercapacitor applications. Electrochimica Acta. 2017;225:493-502.
[20] Sharma PK, Singh MK, Sharma GD, Agrawal A. NiO nanoparticles: facile route synthesis, characterization and potential towards third generation solar cell. Mater Today Proc. 2021;43:3061-3065.
[21] Sabouri Z, Akbari A, Hosseini HA, Darroudi M. Facile green synthesis of NiO nanoparticles and investigation of dye degradation and cytotoxicity effects. J Mol Struct. 2018;1173:931-936.
[22] Thrope B, Ferreira Lima AR, Pinto AH. From the periodic properties of metals to the rietveld refinement of the pharmaceutical molecule naproxen: three remote experiments about x-ray diffraction. J Chem Educ 2022;99:2055-2066.
[23] Bhatti MA, Shah AA, Almani KF, Tahira A, Chalangar SE, dad Chandio A, et al. Efficient photo catalysts based on silver doped ZnO nanorods for the photo degradation of methyl orange. Ceram Int. 2019; 45:23289-23297.
[24] Shimizu S, Matubayasi N. Surface area estimation: replacing the brunauer–emmett–teller model with the statistical thermodynamic fluctuation theory. Langmuir. 2022;38:7989-8002.
[25] Bueno V, Bosi A, Tosco T, Ghoshal S. Mobility of solid and porous hollow SiO2 nanoparticles in saturated porous media: impacts of surface and particle structure. J Colloid Interface Sci. 2022;606:480-490.
[26] Darbandi M, Eynollahi M, Badri N, Mohajer MF, Li ZA. NiO nanoparticles with superior sonophotocatalytic performance in organic pollutant degradation. J Alloys Compd. 2021;889:161706.
[27] Alimohammadi E, Mahdikhah V, Alirezazadeh F, Sheibani S, Farzin YA. Plasmonic resonance and type-I heterojunction interface in SrTiO3/CZTS/Ag nanocomposite for enhanced photocatalytic degradation of organic pollutants. Mater Today Chem. 2023;28:101378.
[28] Nwanya AC, Razanamahandry LC, Bashir AKH, Ikpo CO, Nwanya SC, Botha S, et al. Industrial textile effluent treatment and antibacterial effectiveness of Zea mays L. Dry husk mediated bio-synthesized copper oxide nanoparticles. J Hazard Mater. 2019; 375:281-289.
[29] Ramamoorthy M, Ragupathy S, Sakthi D, Arun V, Kannadasan N. Synthesis of SnO2 loaded on corn cob activated carbon for enhancing the photodegradation of methylene blue under sunlight irradiation. J Environ Chem Eng. 2020;8:104331.
[30] Kamal A, Saleem MH, Alshaya H, Okla MK, Chaudhary HJ, Munis MFH. Ball-milled synthesis of maize biochar-ZnO nanocomposite (MB-ZnO) and estimation of its photocatalytic ability against different organic and inorganic pollutants. J Saudi Chem Soc. 2022;26:101445.